Nosologic imaging of the brain: segmentation and classification using MRI and MRSI

Jan Luts [a,*], Teresa Laudadio [a,b], Albert J. Idema [c], Arjan W. Simonetti [d], Arend Heerschap [e], Dirk Vandermeulen [f], Johan A.K. Suykens [a], Sabine Van Huffel [a]

[a] *Department of Electrical Engineering (ESAT), Research Division SCD, Katholieke Universiteit Leuven, Kasteelpark Arenberg 10, B-3001 Leuven, Belgium*

[b] *Istituto Applicazioni Calcolo, CNR, sez. Bari, via G. Amendola 122/D, I-70126 Bari, Italy*

[c] *Department of Neurosurgery, University of Nijmegen, University Medical Center, Geert Grooteplein Z18, PO Box 9101, 6500 HB Nijmegen, Netherlands*

[d] *Philips Medical Systems, QR-1121, PO Box 10000, 5680 DA Best, Netherlands*

[e] *Department of Radiology, University of Nijmegen, University Medical Center, Geert Grooteplein Z18, PO Box 9101, 6500 HB Nijmegen, Netherlands*

[f] *Department of Electrical Engineering (ESAT), Research Division PSI, Katholieke Universiteit Leuven, Kasteelpark Arenberg 10, B-3001 Leuven, Belgium*

Abstract

A new technique is presented to create nosologic images of the brain based on magnetic resonance imaging (MRI) and magnetic resonance spectroscopic imaging (MRSI). A nosologic image summarizes the presence of different tissues and lesions in a single image by color coding each voxel or pixel according to the histopathological class it is assigned to. The proposed technique applies advanced methods from image processing as well as pattern recognition to segment and classify brain tumours. First, a registered brain atlas and a subject-specific abnormal tissue prior, obtained from MRSI data, are used for the segmentation. Next, the detected abnormal tissue is classified based on supervised pattern recognition methods. Class probabilities are also calculated for the segmented abnormal region. Compared to previous approaches, the new framework is more flexible and able to better exploit spatial information leading to improved nosologic images. The combined scheme offers a new way to produce high-resolution nosologic images, representing tumour heterogeneity and class probabilities, which may help clinicians in decision making.

Key words: brain tumour, nosologic image, magnetic resonance imaging (MRI), magnetic resonance spectroscopic imaging (MRSI), classification, segmentation, class probabilities

List of abbreviations

CCA (canonical correlation analysis); CSF (cerebrospinal fluid); KLR (kernel logistic regression); LDA (linear discriminant analysis); LS-SVM (least squares support vector machine); MCD (minimum covariance determinant); MR (magnetic resonance); MRI (magnetic resonance imaging); MRS (magnetic resonance spectroscopy); MRSI (magnetic resonance spectroscopic imaging); RBF (radial basis function); UMCN (University Medical Center Nijmegen); WHO (World Health Organization);

* Corresponding author. Tel.: +32 16 321065; fax: +32 16 321970

Email adresses: jan.luts@esat.kuleuven.be (Jan Luts), t.laudadio@ba.iac.cnr.it (Teresa Laudadio), a.idema@nch.umcn.nl (Albert J. Idema), arjan.simonetti@philips.com (Arjan W. Simonetti), a.heerschap@rad.umcn.nl (Arend Heerschap), dirk.vandermeulen@esat.kuleuven.be (Dirk Vandermeulen), johan.suykens@esat.kuleuven.be (Johan A.K. Suykens), sabine.vanhuffel@esat.kuleuven.be (Sabine Van Huffel).

.

Introduction

Contrast-enhanced magnetic resonance imaging (MRI) is an important tool for the anatomical assessment of brain tumours. As a consequence, automatic brain tumour segmentation based on MRI is a widely studied topic (1–9). Nowadays, techniques based on thresholding, region growing, clustering, Markov random fields, classification algorithms and artificial neural networks have been used and accurate segmentation results have been reported after comparison with manual tumour segmentation by an expert. However, several diagnostic questions, such as the type and grade of the tumour, are difficult to address using conventional MRI. The histopathological characterization of a tissue specimen remains the gold standard, despite the associated risks of surgery to obtain a biopsy. In recent years, the use of magnetic resonance spectroscopy (MRS), which provides metabolic information, is increasingly being used for more detailed and specific non-invasive evaluation of brain tumours. In particular magnetic resonance spectroscopic imaging (MRSI), which provides quantitative metabolite maps of the brain, is attractive as this may also enable to visualize the heterogeneous spatial extent of tumours, both inside and outside the MRI detectable lesion.

However, the individual inspection and analysis of the many spectral patterns, obtained by MRSI, remains extremely time-consuming and requires specific spectroscopic expertise. Therefore, it is not practical in a clinical setting, where automated processing and evaluation of the MRSI data as well as easy and rapid display of the results as images or maps are needed for routine clinical interpretation of an exam.

As such, the term nosologic image was introduced for an image which indicates a specific tissue type in a certain color (10). Szabo de Edelenyi *et al.* used pattern recognition techniques and combined one specific contrast from MRI with spectroscopic information. Simonetti *et al.* (11) combined additional image variables with the metabolic information to construct nosologic images. Both studies used the combination of MRI and MRSI for new, more relevant brain tumour classifiers, but treated each pixel or voxel of the nosologic image independently, only exploiting the spectral information and image intensities. Therefore, Laudadio *et al.* proposed to apply canonical correlation analysis (CCA) to MRSI data as a way to include spatial information when producing nosologic images (12, 13). Afterwards, Kelm *et al.* (14) suggested to apply conditional random fields to MRSI data since the technique in (12, 13) uses a sliding window which can cancel out effects from isolated voxels and some long-range interactions are lacking because of the fixed window size. Kelm *et al.* claimed that their approach, based on a global method, is able to increase the performance of single voxel classifiers by at least 15 %.

In this paper we extend previous work to construct improved, high-resolution nosologic images. The new scheme benefits from both advanced image processing methods, producing an improved segmented image, and sophisticated classification methods from pattern recognition. The framework comprises a segmentation step and a classification step where MRSI and MRI data are simultaneously exploited, thereby yielding improved segmentation and classification results. Furthermore, spatial information is included in both steps and class probabilities are also generated.

This paper is organized as follows. The Experimental section describes the MRI and MRSI data set, and the two steps of the proposed framework are explained in detail. In the next section the framework is applied to patients' magnetic resonance (MR) data and the results are presented. Finally, the results are discussed and the main conclusions are formulated.

Experimental

Data

In this study, data coming from 24 patients with a brain tumour and 4 healthy volunteers, were selected from the INTERPRET project database (15). The MRI and MRSI data were acquired in the University Medical Center Nijmegen (UMCN). The study was approved by the ethical committee of the UMCN and followed the rules of the World Health Organization (WHO). All data passed a strict quality control and the tumour type was determined by histopathological consensus. To create a sufficiently large training data set for the pattern recognition methods, several voxels, situated in the tumour area, were selected from each patient based on histological, radiological and spectroscopic information (16). Voxels for a specific tissue class were only selected from patients for which this tissue type was confirmed by a histopathological consensus, performed by three independent pathologists. Because of the heterogeneity of brain tumours, the MRI data and the spectral information were taken into account during the selection of voxels. For this purpose, for each patient all the high-resolution MR images were plotted together with the MRSI spectra and a segmented image in which voxels from MRSI were clustered by a model-based algorithm (17) using a graphical user interface. Since the clustering provided an objective segmentation, this was considered to be helpful for voxel selection. Based on all these data sources, an expert in MR spectroscopy selected voxels if they were clearly within the affected brain region, avoiding contamination from normal cerebral tissue, such that the considered spectra were found to be typical for that pathology. Based on the literature (e.g. (18–20)) it is known that normal brain MR spectra typically have a large NAA peak around 2 ppm

and almost equal peaks around 3.2 and 3.03 ppm, respectively choline and creatine. CSF would show no signal in the spectra, but due to partial volume effects, profiles, similar to normal MR spectra, are often visible but with lower intensities. On the other hand, tumour MR spectra have elevated choline compared with creatine. Grade II gliomas have a large myo-inositol peak at 3.57 ppm, elevated choline compared with creatine. Grade III glioma MR spectra have an intermediary pattern between grade II glioma and glioblastoma MR spectra. Glioblastoma MR spectra reveal dominant lipid/lactate peaks around 0.9 and 1.3 ppm. Some high-grade tumours have higher choline, and in general there is a large range of lipid and metabolite concentrations. Meningiomas are characterized by a number of almost equally sized peaks, broad peaks centered around 2.3 and 3.78 ppm, which most likely comprise glutamate, glutamine and macromolecules, choline (3.2 ppm), and various amounts of signal at 0.9 and 1.3 ppm, being macromolecules/lipid/lactate. Following standard radiological MRI features, tumour is normally hypointense on a T1-weighted image and hyperintense on a T2- and proton density-weighted image, while contrast enhancement usually indicates higher grade tissue for gliomas. CSF is hypointense on a T1-weighted image, hyperintense on a T2-weighted image and isointense on a proton density-weighted image. Necrosis is usually hypointense and shows no contrast enhancement. Although this method was subjective, it was chosen because tumours are known to be heterogeneous and because there is no "ground truth" in the diagnosis of brain tumours at the voxel level. Also, spectra from cerebrospinal fluid (CSF) and normal tissue measured from volunteers and patients were selected. Six classes of pathology were considered: normal brain tissue from volunteers and apparently normal tissue from the contralateral half of the brain of patients (218 voxels from 8 persons), CSF (100 voxels from 8 patients), grade II glioma (176 voxels from 10 patients), grade III glioma (69 voxels from 5 patients), grade IV glioma (70 voxels from 7 patients) and meningioma (48 voxels from 3 patients).

The data were acquired on a 1.5 T Siemens Vision Scanner with CP-head coil. Four MR images were acquired, namely T1-weighted image (TE/TR = 15/644ms), T2-weighted image (TE/TR = 98/3100ms), proton density-weighted image (TE/TR = 16/3100ms) and gadolinium enhanced T1-weighted image (15 ml 0.5 M Gd-DTPA), with matrix size equal to 256 × 256. Both water-suppressed and unsuppressed proton MR spectroscopic images were measured using a 2D STEAM sequence with the STEAM box positioned totally in the brain (16 × 16 × 1024 samples, TR/TE/TM = 2000 or 2500/20/30 ms, slice thickness = 12.5 or 15 mm, FOV = 200 mm, spectral width = 1000 Hz and NS = 2). Disturbing signals arising from the fat tissue surrounding the skull were avoided. The location of the STEAM box was determined using the gadolinium enhanced T1-weighted image showing the largest tumour area. The MRSI slice was centered around an MRI slice of 5 mm.

MR image registration was performed based on the algorithm described in (21).

It was assumed that the MRSI data were registered with the proton density-weighted image since they were acquired in a consecutive manner. Preprocessing of MRSI included filtering of k-space data by a Hanning filter of 50 % using the LUISE software package (Siemens, Erlangen, Germany), zero filling to 32 $\times$ 32, spatial 2D Fourier transformation to obtain time domain signals for each voxel, correction for eddy current effects by a technique which prevents occasional occurrence of eddy current correction induced artifacts (22, 23), frequency alignment, water removal using HLSVD from 4.3 ppm to 5.5 ppm (24) and a simple baseline correction using an exponential filter with a width of 5 ms followed by subtraction of the residual of the original signal. All first order phases were corrected by first manually optimizing the mean spectrum which was calculated from all spectra in the STEAM box of each patient's MRSI data. Next, this correction was applied to each separate signal of the patient's MRSI data. Finally, the spectra were normalized using the water signal. For each metabolite signal, a corresponding water-unsuppressed signal was available, acquired with the same acquisition parameters as the metabolite signal and originating from the same voxel. The amplitude of the water-unsuppressed signal was estimated by a nonlinear least squares algorithm (25). The water-unsuppressed signal was modeled in the time domain by a Voigt model, with an additional first order term that corrected for eddy currents. HSVD was used to obtain initial parameter estimates, which were subsequently used as starting values in a nonlinear least squares algorithm to obtain the final parameter estimates. Each spectral value in the preprocessed water-suppressed spectrum was divided by the obtained estimate of the intensity of the water peak.

In this study an input pattern for pattern recognition was either a full spectrum or a set of features extracted from the spectrum in combination with MRI pixel intensities. The magnitude spectrum was computed and the spectral points within the frequency range (0.5-4 ppm) were used as input for some of the classification problems in the former case. Figure 1 depicts the water-normalized mean magnitude spectra, along with the standard deviation, for each of the tissue types in the data set. Concerning the feature-based approach, ten different features were extracted, using peak integration within a spectral range, from each spectrum (26): lipids (0.835-0.965 ppm), lipids (1.2 ppm) and lactate + alanine (1.265-1.395 ppm), N-acetylaspartate (1.955-2.085 ppm), glutamate + glutamine (2.135-2.265 ppm), creatine (2.955-3.095 ppm), choline (3.135-3.265 ppm), taurine + glucose (3.375-3.505 ppm), myo-inositol + glycine (3.495-3.625 ppm), glutamate + glutamine + alanine (3.685-3.815 ppm) and creatine (3.885-4.015 ppm). These ten values, referred to as the peak-integrated values in the rest of the paper, were combined with four MRI variables obtained by lowering the resolution of the four MR images to the one of the MRSI grid by averaging pixel intensities within each voxel as in (11).

A two-step segmentation-classification framework

In this paper, we propose a two-step segmentation-classification framework able to simultaneously exploit MRI and MRSI data. In particular, the first step was performed based on the segmentation method presented by Prastawa *et al.* in (27). The required input for that method was a T2-weighted image. No contrast-enhanced images were needed, but, additional types of MR images could be used to improve the segmentation. More precisely, Prastawa *et al.* proposed a method consisting of three stages: abnormality detection using a digital brain atlas and outlier detection; edema detection based on the T2-weighted image intensities; application of geometric and spatial constraints to the detected edema and tumour regions. In our new framework, we included additional information from MRSI to improve the abnormal tissue detection for segmentation. Specifically, as described in the next section, in addition to the standard brain atlas, a subject-specific abnormal tissue prior was generated by applying a supervised pattern recognition technique to the available MRSI (and MRI) data set. In the second step of the segmentation-classification framework all pixels from the detected abnormal region were classified based on supervised pattern recognition techniques and nosologic images were provided as final result, where each tissue type was denoted by a specific color. The two-step framework is explained in the following paragraphs. For the sake of completeness, the considered segmentation and pattern recognition algorithms are described in more detail in the Appendix section.

MRI segmentation

Generating a subject-specific abnormal tissue prior from MRSI and MRI

In a digital brain atlas, only probabilities are provided for the healthy tissue classes: white matter, gray matter and CSF. The study in (28) proposed to include a subject-specific abnormal tissue prior by means of the contrast-enhanced image. In our study, we generated a subject-specific prior for the abnormal tissue as well, but based on a linear discriminant analysis (LDA) classifier. Indeed, in (29) it was shown that a simple linear classifier was sufficient to separate abnormal tissue from healthy tissue. Therefore, we applied LDA (trained on all available training data except data coming from the case under study) to the grid of feature vectors containing fourteen entries, i.e. ten bicubically interpolated peak-integrated values (such that it matched with the size of the MRI grid) and the four types of MRI pixel intensities. For each pixel within the area of the STEAM box, it was predicted whether there was abnormal or healthy tissue based on all peak-integrated values and the MRI

pixel intensities. The right panel of Figure 2 depicts the resulting grid that was generated by the LDA classifier for case 6. For illustration purposes, the choline over creatine ratio, obtained by the interpolated peak-integrated values, is also depicted in the middle image.

Next, the output from LDA was integrated into the original digital brain atlas by setting the abnormal prior, if abnormal tissue was predicted by the LDA method, to a probability derived from that classifier. If no abnormal tissue was predicted by LDA, the abnormal prior was set to a fraction of the white matter and gray matter atlas probabilities as in (27). Since the MRSI information was restricted to the STEAM box, the abnormal tissue prior was only available within that area. Every prior probability outside that box was obtained as in (27). In the results section it is demonstrated that the addition of the abnormal tissue prior improves the segmentation procedure.

Segmentation based on the modified atlas

After the prior was generated, part of the segmentation approach from (27) was followed. Abnormal tissue was detected using an iterative procedure. First the posterior probabilities, or atlas probabilities in the first iteration, were thresholded and pixels in high confidence regions were sampled. Next, the samples from normal tissue that exceeded a distance threshold, based on the minimum covariance determinant (MCD) estimator, were removed. A non-parametric model was used to estimate the probability density functions from the samples. The posterior probabilities were calculated based on the subject-specific atlas priors and the estimated densities. To conclude an iteration of abnormality detection, a bias field correction was performed because of the presence of the image inhomogeneity. The bias field was estimated from the white and gray matter probabilities and the full procedure was repeated. After the separation of abnormality, an edema detection stage was proposed in the framework in (27). The detection was done using the T2-weighted image, assuming that edema has high fluid content and appears brighter than the tumour. We decided to remove this stage from our segmentation step since, after validation of the results, it seemed that cysts, which were also brighter on the T2 image, were often segmented as edema. Also, it is known that edema in glioma tumours is often infiltrated and therefore this tissue should be detected as abnormal. The last stage of the segmentation step was reclassification with spatial and geometric constraints. For this purpose region competition snakes were used (30). First, the procedure for the last stage thresholded and sampled the posterior probabilities. The tumour samples were pruned based on the level-set evolution after which the densities were estimated. New posterior class probabilities were calculated; the bias field was corrected and the procedure

was repeated.

Classification of the abnormal region

Determination of the type of abnormal tissue

After segmentation, white matter, gray matter, CSF and abnormal tissue were separated. To provide additional information about the tumour type that was present within the abnormal tissue region, a supervised pattern recognition step was introduced. As for the subject-specific abnormal tissue prior, the MRSI data (e.g. spectra, peak-integrated values) were interpolated to match the size of the MRI data. Naturally, only pixels within the STEAM box could be classified. More precisely, all pixels, found to be abnormal by the segmentation step, were classified into one of the tumour categories that were represented in the training set for pattern recognition. This means that for this specific study, we were able to detect white matter, gray matter, CSF, and, based on spectroscopic profiles, grade II glioma, grade III glioma, grade IV glioma and meningioma.

Pattern recognition methods

Concerning classification, basically every (semi-)supervised pattern recognition method can be incorporated, which makes the framework very flexible. Here, we decided to focus on kernel logistic regression (KLR) (31, 32), a multiclass classifier using Bayesian least squares support vector machines (LS-SVMs) (29) and CCA. Bayesian LS-SVMs (33) and KLR were used since these kernel-based methods were able to provide class probabilities instead of 'black or white' decisions. CCA was included because it was capable to exploit spatial information (12, 13). The methods are briefly discussed in the following paragraph.

Standard LS-SVMs (34, 35) can only handle binary classification problems and produce binary output scores. In (29) it was proposed to combine binary Bayesian LS-SVMs with radial basis function (RBF) kernel into a multiclass classifier system. Based on binary classifiers and pairwise combination algorithms multiclass class probabilities were retrieved. Following the findings in (29), the combination method of Wu *et al.* (36) was used to combine pairwise class probabilities. Direct multiclass class probabilities were generated using KLR. In (32), it was shown that the optimization problem for KLR could be solved by a weighted version of LS-SVMs. From the practical point of view this means that KLR does not need to construct binary classifiers;

one direct multiclass solution can be obtained. Finally, CCA was included since the method exploits spatial information, i.e. based on the information in the neighbouring pixels, a decision is made for the center pixel. Since CCA was applied to the interpolated grid (within the abnormal tissue region), we reduced the risk to average out the effect of isolated tumour voxels by the information that was present in the neighbourhood as compared to (12, 13). The symmetric 3×3 model without corner voxels was used as spatial model and PCA was applied as subspace model.

Results

A leave-one-person-out validation analysis was performed to evaluate the framework. For the creation of the abnormal tissue prior and for the classification step, all data from the test subject were removed from the training set. As such, model selection was performed on all data except for the voxels coming from the subject under study. In the next paragraph nosologic images are reported and the use of class probabilities is illustrated. Finally, the use of the abnormal tissue prior is explained. Table 1 provides an overview of the patients' data.

Analysis of the patient data

The framework was applied to generate nosologic images for 10 patients (Figures 3 - 9). Light blue reflects white matter, dark blue gray matter, green csf, yellow grade II glioma, orange grade III glioma, dark red glioblastoma and purple meningioma. All classification results in this section were generated using feature vectors where peak-integrated values were combined with image intensities. To demonstrate the flexibility of the framework, and more specifically the flexibility of the classification step, the use of various pattern recognition methods is illustrated. Nevertheless, it is worth stressing that the goal of the present study is not to compare the different pattern recognition methods, but to show that any type of classifier can be integrated in the classification step, or can be used for generating the additional subject-specific abnormal tissue prior in the segmentation step. The flexibility property shown here is very important as, based on the specific problem under investigation, ad hoc classification methods could be applied.

Cases 9, 8 and 10 represent patients with a glioblastoma multiforma tumour as assigned by the pathologists. The nosologic images, obtained by applying a Bayesian LS-SVM classifier, show that the method was able to detect the tumour lesions and glioblastoma tissue (Figures 3 and 4). These examples

also show that edema and/or tumour infiltration is difficult to assess. In diffuse astrocytoma, the peritumoural edema is presumed infiltrated by glioma tumour cells. In these cases the differentiation between pure infiltration and pure edema can not be made. As discussed before the segmentation of edema was not consistent and was left out of the procedure and so no edema is shown in the nosologic images. In heterogeneous tumours, like gliomas, this difference indeed can not be made with conventional MRI techniques. Therefore, the most likely assignment for this abnormal tissue is low grade glioma. Low grade tumour next to glioblastoma is pathologically possible. In case 10, there are two tumour areas. The posterior part could include a hematoma within the tumour. For the surrounding tissue it is difficult to distinguish edema from infiltrating tumour.

Cases 4, 6 and 7 are good examples of the difficult differentiation between WHO grade II and grade III glioma brain tumour (Figures 5 - 7). The histopathological diagnosis for case 4 was grade II glioma. The framework, applying CCA in the classification step, found the correct tissue type, despite the enhancement after contrast for small parts of the tumour at the occipital parts of the insula (Figure 5). For case 6 the pathologists disagreed between a grade II and a grade III glial tumour. The nosologic image, created using a Bayesian LS-SVM classifier, shows a heterogeneous tumour with mainly grade III glioma, according to the spectroscopic classifier, especially in the part with enhancement after gadolinium (Figure 6). The differentation between grade II glioma and edema at the frontal and medial parts can not be made. For case 7 with an anaplastic oligodendroglioma, CCA was used (Figure 7). Almost only low grade glioma, WHO grade II was found with a small region of anaplastic glioma, WHO grade III. This would be an underestimation of the real situation. At surgery, a debulking of the tumour was performed. Therefore, the pathological diagnosis was not from only the small part with a nosological anaplastic tumour.

Case 3 is a diffuse low grade astrocytoma, grade II, with no enhancement after contrast and good segmentation of the tumour/tumour infiltration/edema based on KLR (Figure 8). For case 2 the histopathological agreement was grade II glioma, despite the enhancement after gadolinium (Figure 9). The Bayesian LS-SVM method was used and it detected the correct tissue type. However, in this case no edema and/or tumour infiltration was detected which was very reliable around the enhancing spot. The nosologic image for case 11 with a meningioma tumour was obtained by the CCA classifier (Figure 9). In this case the small edema part at the occipital part of the tumour was not classified as abnormal tissue. In the case of a low grade meningioma there is no infiltration.

Class probabilities

The use of class probabilities is illustrated for three patients (Figures 10 - 11). The histopathology for case 5 was grade II glioma and the result in the middle panel was obtained using a KLR classifier (Figure 10). As input for the classifier the magnitude spectra were used. It seems that a region of grade III glioma was found at the top of the tumour. The right panel was constructed by only considering pixels for which the probability of the classification result was more than 60 %. If the probability for a pixel was lower than 60 %, the pixel was left black. In the resulting image one can observe that the classifier is more sure about the grade II glioma pixels and the region of grade III glioma is now entirely dropped. It is possible to generate probability maps for various tissue types. In Figure 11 a probability map and a contour plot are depicted for case 6. The lighter the probability map is, the higher the probability for grade III glioma. Blue contour lines show higher grade III glioma probabilities as opposed to red contour lines. The grade III glioma probabilities are higher at the frontal part of the abnormal tissue region with the enhancement after gadolinium and smaller at the occipital part of the tumour in case 6. Figure 11 also depicts the correlation coefficients generated by CCA for grade III glioma in a map and contour plot for case 7. The correlation coefficients are higher in the center and at the medial part of the tumour.

Subject-specific abnormal tissue prior

During the detection of abnormality step a sampling for gray matter, white matter and CSF was done based on the atlas priors (Figure 12). On the left the T2-weighted images for cases 1, 4, 5 and 6 are depicted. The middle images show which pixels were sampled for the healthy tissue classes (i.e. gray matter, white matter and CSF) following the standard digital brain atlas, as proposed in (27), for all four cases. It can be observed that for all cases samples for healthy tissue were picked from the tumour area. This contamination can be rather strong as for instance for case 4. On the other hand, the images on the right show which samples were picked for the healthy tissue classes after the subject-specific abnormal tissue prior was added to the standard atlas. The above mentioned figure clearly shows that the extra prior improves the sampling and, as a consequence, reduces the contamination reported in (27). As a result, improved sampling leads to higher quality prototypes for all the tissue classes and better density estimates in the detection of the abnormality step. Finally, an example (case 4) of the difference between the two approaches with respect to the final segmentation is provided (Figure 13). In contrast to the panels on the right, no abnormal tissue prior was added to the digital brain atlas to produce the left images. The top row summarizes the information that

was available in the atlas before starting segmentation. This result was generated by choosing the tissue type with the highest prior probability based on the (modified) atlas. The lower row shows the final result after segmentation. CSF is colored green, white matter light blue, gray matter dark blue and abnormal tissue is red. Before starting segmentation, one can observe that there was only a region for which the probabilities of abnormal tissue were higher than the ones of the normal classes in the digital brain atlas that was modified with the subject-specific abnormal tissue prior. After segmentation, and when comparing with the MRI of case 4 (Figure 5) only a small part of the abnormal tissue region was detected by the original segmentation algorithm that just included healthy tissue priors. By introducing the extra prior from MRSI, the abnormal tissue region was better recognized. The MR spectra confirmed the existence of abnormal tissue in that area (Figure 5).

Discussion

In MRI-based segmentation of tissue in the brain, a digital brain atlas is an important, additional, tool to resolve the problem of overlap between intensity distributions of different tissue types. Since a digital brain atlas only contains priors for the healthy tissue classes, researchers attempted to include a prior for the abnormal tissue as well. Typically, the contrast-enhanced T1-weighted image is used for this purpose (28). However, it is known that blood vessels also generally appear enhanced. In addition, tumours may show only partially signal enhancement and some tumours do not enhance at all. For example, in this particular study we observed no enhancement for case 3 (Figure 8). For this reason, we decided to use the MRSI data to generate the prior for tissue abnormality. Although the spatial resolution of MRSI is low compared to MRI, it appeared that MRSI was very useful to define the prior and that it could improve the original segmentation algorithm described in (27). Indeed, in this study of Prastawa *et al.* it was explained that the segmentation algorithm could only deal with a limited amount of brain deformation. During the detection of abnormality step the atlas is sampled. The outliers are detected based on the MCD method and the density functions are estimated. However, when there is a serious brain deformation, the brain atlas leads to incorrect sampling since pixels for the healthy tissue classes are sampled from the abnormal tissue regions. In this case the samples are severely contaminated and the MCD algorithm may not yield correct results, leading to incorrect estimated densities. Figures 12 and 13 illustrate this and show that the use of the abnormal tissue prior, generated from MRSI, is advantageous.

In general, the proposed framework highlights the advantages of a method able to exploit and combine different types of information. In particular, our studies show the value of adding MRSI over MRI data, of adding MRI over

MRSI information, and the improvements achieved in the segmentation and classification approaches with respect to their previously proposed versions. For instance, several diagnostic questions, such as the type and grade of the tumour, are difficult to address using MRI, but, MRSI data enable to take the corresponding metabolic differences into account. Therefore, using MRSI information over just MRI has the additional advantage that nosologic images (specifying the type of the tumour) can be obtained, instead of the results (which only localize the tumour) obtained with classical MRI segmentation approaches as in (27).

The added value of MRI over just MRSI has already been evaluated in a number of studies, which concluded that combining MRI with MRSI features improved the performance of the classifiers (16, 37, 38). For this reason, in the present study, the four MR images were also used in the classification step. Furthermore, adding MRI over MRSI data, allowed to perform the segmentation step based on high-resolution MRI data. We found that this improved the detection of CSF compared to pure segmentation of MRSI data and also gray matter and white matter were detected based on MRI. On the contrary, the CCA approach in (12, 13) only performed a segmentation on the MRSI data. CCA is an interesting method since it is able to simultaneously exploit the spectral-spatial information provided by the MRSI data and is computationally efficient. On the other hand, the disadvantage of this approach is that the same spatial constraints (i.e. a fixed spatial model) are used for every voxel of the MRSI grid, without taking into account whether the voxel is on the border or the middle of the tumour. In simulation studies we experienced that this can lead to wrong classifications for rather isolated tumour voxels. In the proposed framework, CCA was applied after the segmentation step, i.e. after the tumour was detected, reducing the risk of misclassification for rather isolated tumour voxels. Therefore, the above issue is improved by making use of image processing methods, that incorporate more advanced spatial constraints, based on the high-resolution MRI data. The use of these spatial constraints in the current method is also an improvement compared to the approaches where every pixel or voxel was classified separately, ignoring this prior knowledge (10, 11, 29).

On the other hand, as proven by biopsies, outside the abnormal tissue on the conventional MRI infiltrating tumour cells can be found with and without abnormal spectroscopic findings (39–42). Therefore, the whole infiltrating tumour is not always taken into account. Price *et al.* showed a biopsy-guided improved delineation of glioma tumours with diffusion tensor imaging (39). Also, the segmentation of edema in glioma tumours is not straightforward. To distinguish edema from tumour the intensity of a T2-weighted image is not sufficient. This does not always differentiate tumour cysts, resection cysts or cerebral fluid from pure edema. Next to this, in glioma tumours the peritumoural edema is mostly infiltrated by tumour cells and the intensity differences

between edema and tumour are on a sliding scale. With the available information in this study no specific segmentation of peritumoural edema and tumour could be made for glioma tumours. Therefore, this segmentation step was not used. Ricci *et al.* showed metabolic changes in peritumoural edema with MR spectroscopy (43). The combination of diffusion tensor imaging and MR spectroscopy might be helpful to improve the delineation of glioma tumours and differentiation of edema and infiltrating tumour.

The difference between WHO grade II and grade III is radiologically very difficult. According to the WHO-2007 classification (44), the main histopathological difference between WHO grade II and III diffuse astrocytic neoplasms is increased mitotic activity in the latter. Therefore, it is not surprising that one third of the non-enhancing diffuse gliomas are histopathologically diagnosed as high-grade lesions at the time of biopsy (45). The value of the addition of MR spectroscopy for the differentiation of WHO grade II and grade III gliomas is currently not clear (46, 47). However, in part this could be due to the underestimation of the brain tumour malignancy in tumours diagnosed by biopsies (48). By including perfusion and diffusion MR data the differentiation may be improved (49, 50).

Although precise estimation of peak integrals is difficult due to peak overlap and noise, features were extracted from the spectra based on simple peak integration. Therefore, spectral fitting methods might seem more appropriate. However, prior to the application of the two-step framework, the classification accuracies of different spectral fitting methods and peak integration were compared. Since the quantification approaches did not improve classifier performance and since these methods were more time-consuming, we decided to use peak integration. Some previous studies also reported no increase in classifier performance for quantification methods compared to automated approaches as for instance principal component analysis (14, 37). A related issue is determining the number of features to extract from the spectra. In this study we extracted a common set of features which are in general known to be relevant for the classification problems under study. Although the focus of the present work was the development of the methodology of the framework, this is an issue that can be improved and it is still open for discussion. As such, future work could focus on the optimization of these data preprocessing steps as this can potentially further increase the performance of the total framework that is presented here.

In this study only one of the MRI slices was totally included within the MRSI slice. For this reason, the framework only combined one MRI slice with the MRSI data. However, in practice, depending on its size, multiple MRI slices may be needed to cover the whole tumour. As such, a potential improvement of the existing framework could be the extension to three-dimensional MRSI data with the inclusion of multiple MRI slices. Also, in the present study

the standard image orientation protocol in the radiology service was used in order to limit the acquisition time. If a different orientation is used, a better enclosure of the brain tumour mass may be obtained, such that the framework that is presented here provides further improved nosologic images.

Conclusions

This paper proposes a new method to generate nosologic images of the brain by exploiting and combining MRI and MRSI data. Advanced methods from image processing and pattern recognition are combined in a two-step approach. In the first step segmentation is performed by means of a modified version of the method described in (27), by including a subject-specific abnormal tissue prior, derived from MRI and MRSI, in the original brain atlas. The subject-specific abnormal tissue prior is found to improve the segmentation procedure. The segmentation step provides an image of the slice of interest where white matter, gray matter, CSF and the abnormal region are clearly visualized. Next, the abnormal tissue is classified using pattern recognition and class probabilities are generated for the diverse tissue types. The method is applied to various patients with different types of brain tumours. Compared to previous approaches that generate nosologic images, the use of spatial information and prior knowledge is further improved in the proposed method. The framework offers a new way to visualize tumour heterogeneity and class probabilities in a single nosologic image, assisting clinicians in decision making.

Acknowledgements

This research is funded by a PhD grant of the Institute for the Promotion of Innovation through Science and Technology in Flanders (IWT-Vlaanderen); Research supported by Research Council KUL: GOA-AMBioRICS, several PhD/postdoc & fellow grants, Centers-of-excellence optimisation, IDO 05/010 EEG-fMRI, GOA/2004/05 (Mixing and Analyzing Real and Virtual Environments and Lighting); Institute for Molecules and Materials, Analytical Chemistry, Chemometrics Research Department of the Radboud University Nijmegen for preprocessing the MRSI data; Maarten Aerts for the implementation of the basic segmentation algorithm; Flemish Government: FWO: PhD/postdoc grants, projects, G.0360.05 (Advanced EEG analysis techniques for epilepsy monitoring), G.0519.06 (Noninvasive brain oxygenation), G.0341.07 (Data fusion), G.0321.06 (Numerical tensor techniques for spectral analysis), G.0302.07 (Support vector machines and kernel methods), G.0566.06 (Computational strategies for shape modeling and matching and their application in medical image analysis), research communities (ICCoS, ANMMM); IWT: PhD

Grants; Belgian Federal Government: DWTC (IUAP IV-02 (1996-2001), IUAP V-22 (2002-2006): Dynamical Systems and Control: Computation, Identification & Modelling) and Belgian Federal Science Policy Office IUAP P6/04 (Dynamical systems, control and optimization, 2007-2011); EU: use of the data provided by the EU funded INTERPRET project (contract no. IST-1999-10310) is gratefully acknowledged, Marinette van der Graaf is gratefully acknowledged, BIOPATTERN (contract no. FP6-2002-IST 508803), eTUMOUR (contract no. FP6-2002-LIFESCIHEALTH 503094), HealthAgents (contract no. FP6-2005-IST 027213), FAST (contract no. FP6-019279-2), ESA: Cardiovascular Control (Prodex-8 C90242).

References

[1] Warfield SK, Kaus M, Jolesz FA, Kikinis R, Adaptive template moderated spatially varying statistical classification. In *Lecture Notes In Computer Science, International Conference on Medical Image Computing and Computer-Assisted Intervention*, volume 1496, Springer-Verlag, London, volume 1496. 1998; 431–438.

[2] Clark MC, Hall LO, Goldgof DB, Velthuizen R, Murtagh FR, Silbiger MS, Automatic tumor segmentation using knowledge-based techniques. *IEEE Transactions on Medical Imaging*. 1998; **17**: 187–201.

[3] Van Leemput K, Maes F, Vandermeulen D, Suetens P, Automated model-based tissue classification of MR images of the brain. *IEEE Transactions on Medical Imaging*. 1999; **18**: 897–908.

[4] Kaus M, Warfield SK, Nabavi A, Chatzidakis E, Black PM, Jolesz FA, Kikinis R, Segmentation of meningiomas and low grade gliomas in MRI. In *Lecture Notes In Computer Science, International Conference on Medical Image Computing and Computer-Assisted Intervention*, volume 1679, Springer-Verlag, London, volume 1679. 1999; 1–10.

[5] Fletcher-Heath LM, Hall LO, Goldgof DB, Murtagh FR, Automatic segmentation of non-enhancing brain tumors in magnetic resonance images. *Artificial Intelligence in Medicine*. 2001; **21**: 43–63.

[6] Kaus M, Warfield SK, Nabavi A, Black PM, Jolesz FA, Kikinis R, Automated segmentation of MRI of brain tumors. *Radiology*. 2001; **218**: 586–591.

[7] Gering DT, Grimson WEL, Kikinis R, Recognizing deviations from normalcy for brain tumor segmentation. In *Lecture Notes In Computer Science, International Conference on Medical Image Computing and Computer-Assisted Intervention*, volume 2488, Springer-Verlag, London, volume 2488. 2002; 388–395.

[8] Cuadra MB, Gomez J, Hagmann P, Pollo C, Villemure J-G, Dawant BM, Thiran J-P, Atlas-based segmentation of pathological brains using a model of tumor growth. In *Lecture Notes In Computer Science, International Conference on Medical Image Computing and Computer-Assisted Intervention*, volume 2488, Springer-Verlag, London, volume 2488. 2002; 380–387.

[9] Schmidt M, Levner I, Greiner R, Murtha A, Bistritz A, Segmenting brain tumors using alignment-based features. In *International Conference on Machine Learning and Applications*, IEEE Computer Society, Washington. 2005; 215–220.

[10] Szabo de Edelenyi F, Rubin C, Esteve F, Grand S, Decorps M, Lefournier V, Le Bas JF, Remy C, A new approach for analyzing proton magnetic resonance spectroscopic images of brain tumors: nosologic images. *Nature Medicine*. 2000; **6**: 1287–1289.

[11] Simonetti AW, Melssen WJ, van der Graaf M, Heerschap A, Buydens LMC, A new chemometric approach for brain tumor classification us-

ing magnetic resonance imaging and spectroscopy. *Analytical Chemistry*. 2003; **75**: 5352–5361.

[12] Laudadio T, Pels P, De Lathauwer L, Van Hecke P, Van Huffel S, Tissue segmentation and classication of MRSI data using canonical correlation analysis. *Magnetic Resonance in Medicine*. 2005; **54**: 1519–1529.

[13] Laudadio T, Martinez-Bisbal MC, Celda B, Van Huffel S, Fast nosological imaging using canonical correlation analysis of brain data obtained by two-dimensional turbo spectroscopic imaging. *Nuclear Magnetic Resonance in Biomedicine*. 2008; **21**: 311–321.

[14] Kelm BM, *Evaluation of vector-valued clinical image data using probabilistic graphical models: quantification and pattern recognition*. Ph.D. thesis, University of Heidelberg. 2007.

[15] International Network for Pattern Recognition of Tumours Using Magnetic Resonance.
URL `http://azizu.uab.es/INTERPRET/ (Accessed: 29 January 2008)`

[16] Devos A, Simonetti AW, van der Graaf M, Lukas L, Suykens JAK, Vanhamme L, Buydens LMC, Heerschap A, Van Huffel S, The use of multivariate MR imaging intensities versus metabolic data from MR spectroscopic imaging for brain tumour classification. *Journal of Magnetic Resonance*. 2005; **173**: 218–228.

[17] Wehrens R, Simonetti AW, Buydens LMC, Mixture modelling of medical magnetic resonance data. *Journal of Chemometrics*. 2002; **16**: 274–282.

[18] Tate AR, Underwood J, Acosta DM, Julia-Sape M, Majos C, Moreno-Torres A, Howe FA, van der Graaf M, Lefournier V, Murphy MM, Loosemore A, Ladroue C, Wesseling P, Bosson J-L, Cabanas ME, Simonetti AW, Gajewicz W, Calvar J, Capdevila A, Wilkins PR, Bell BA, Remy C, Heerschap A, Watson D, Griffiths JR, Arus C, Development of a decision support system for diagnosis and grading of brain tumours using in vivo magnetic resonance single voxel spectra. *Nuclear Magnetic Resonance in Biomedicine*. 2006; **19**(4): 411–434.

[19] Howe FA, Opstad KS, 1H MR spectroscopy of brain tumours and masses. *Nuclear Magnetic Resonance in Biomedicine*. 2003; **16**: 123–131.

[20] Howe FA, Barton SJ, Cudlip SA, Stubbs M, Saunders DE, Murphy M, Wilkins P, Opstad KS, Doyle VL, McLean MA, Bell BA, Griffiths JR, Metabolic profiles of human brain tumors using quantitative in vivo 1H magnetic resonance spectroscopy. *Magnetic Resonance in Medicine*. 2003; **49**: 223–232.

[21] Maes F, Collignon A, Vandermeulen D, Marchal G, Suetens P, Multimodality image registration by maximization of mutual information. *IEEE Transactions on Medical Imaging*. 1997; **16**: 187–198.

[22] Klose U, In vivo proton spectroscopy in presence of eddy currents. *Magnetic Resonance in Medicine*. 1990; **14**: 26–30.

[23] Simonetti AW, Melssen WJ, van der Graaf M, Heerschap A, Buydens LMC, Automated correction of unwanted phase jumps in reference signals

which corrupt MRSI spectra after eddy current correction. *Journal of Magnetic Resonance*. 2002; **159**: 151–157.

[24] Pijnappel WWF, van den Boogaart A, de Beer R, van Ormondt D, SVD-based quantification of magnetic resonance signals. *Journal of Magnetic Resonance*. 1992; **97**: 122–134.

[25] Devos A, Lukas L, Suykens JAK, Vanhamme L, Tate AR, Howe FA, Majos C, Moreno-Torres A, van der Graaf M, Arus C, Van Huffel S, Classification of brain tumours using short echo time 1H MR spectra. *Journal of Magnetic Resonance*. 2004; **170**: 164–175.

[26] Govindaraju V, Young K, Maudsley AA, Proton NMR chemical shifts and coupling constants for brain metabolites. *Nuclear Magnetic Resonance in Biomedicine*. 2000; **13**: 129–153.

[27] Prastawa M, Bullitt E, Ho S, Gerig G, A brain tumor segmentation framework based on outlier detection. *Medical Image Analysis*. 2004; **8**: 275–283.

[28] Prastawa M, Bullitt E, Moon N, Van Leemput K, Gerig G, Automatic brain tumor segmentation by subject specific modification of atlas priors. *Academic Radiology*. 2003; **10**: 1341–1348.

[29] Luts J, Heerschap A, Suykens JAK, Van Huffel S, A combined MRI and MRSI based multiclass system for brain tumour recognition using LS-SVMs with class probabilities and feature selection. *Artificial Intelligence in Medicine*. 2007; **40**: 87–102.

[30] Ho S, Bullitt E, Gerig G, Level-set evolution with region competition: Automatic 3-D segmentation of brain tumors. In *International Conference on Pattern Recognition*, IEEE Computer Society, Washington. 2002; 532–535.

[31] Zhu J, Hastie T, Kernel logistic regression and the import vector machine. *Journal of Computational & Graphical Statistics*. 2005; **14**(1): 185–205.

[32] Karsmakers P, Pelckmans K, Suykens JAK, Multi-class kernel logistic regression: a fixed-size implementation. In *International Joint Conference on Neural Networks*, Orlando. 2007; 1756–1761.

[33] Van Gestel T, Suykens JAK, Lanckriet G, Lambrechts A, De Moor B, Vandewalle J, Bayesian framework for least squares support vector machine classifiers, Gaussian processes and kernel Fisher discriminant analysis. *Neural Computation*. 2002; **14**: 1115–1147.

[34] Suykens JAK, Vandewalle J, Least squares support vector machine classifiers. *Neural Processing Letters*. 1999; **9**(3): 293–300.

[35] Suykens JAK, Van Gestel T, De Brabanter J, De Moor B, Vandewalle J, *Least Squares Support Vector Machines*. World Scientific, Singapore. 2002.

[36] Wu T, Lin C, Weng R, Probability estimates for multi-class classification by pairwise coupling. *Journal of Machine Learning Research*. 2004; **5**: 975–1005.

[37] Simonetti AW, Melssen WJ, Szabo de Edelenyi F, van Asten JJA, Heerschap A, Buydens LMC, Combination of feature-reduced MR spectro-

scopic and MR imaging data for improved brain tumor classification. *Nuclear Magnetic Resonance in Biomedicine*. 2005; **18**: 34–43.

[38] Galanaud D, Nicoli F, Chinot O, Confort-Gouny S, Figarella-Branger D, Roche P, Fuentes S, Le Fur Y, Ranjeva J-P, Cozzone PJ, Noninvasive diagnostic assessment of brain tumors using combined in vivo MR imaging and spectroscopy. *Magnetic Resonance in Medicine*. 2006; **55**: 1236–1245.

[39] Price SJ, Jena R, Burnet NG, Hutchinson PJ, Dean AF, Pena A, Pickard JD, Carpenter TA, Gillard JH, Improved delineation of glioma margins and regions of infiltration with the use of diffusion tensor imaging: An image-guided biopsy study. *American Journal of Neuroradiology*. 2006; **27**: 1969–1974.

[40] Croteau D, Scarpace L, Hearshen D, Gutierrez J, Fisher JL, Rock JP, Mikkelsen T, Correlation between magnetic resonance spectroscopy imaging and image-guided biopsies: Semiquantitative and qualitative histopathological analyses of patients with untreated glioma. *Neurosurgery*. 2001; **49**: 823–829.

[41] Ganslandt O, Stadlbauer A, Fahlbusch R, Kamada K, Buslei R, Blumcke I, Moser E, Nimsky C, Proton magnetic resonance spectroscopic imaging integrated into image-guided surgery: correlation to standard magnetic resonance imaging and tumor cell density. *Neurosurgery*. 2005; **56**: 291–298.

[42] Li X, Lu Y, Pirzkall A, McKnight TR, Nelson SJ, Analysis of the spatial characteristics of metabolic abnormalities in newly diagnosed glioma patients. *Journal of Magnetic Resonance Imaging*. 2002; **16**: 229–237.

[43] Ricci R, Bacci A, Tugnoli V, Battaglia S, Maffei M, Agati R, Leonardi M, Metabolic findings on 3T 1H-MR spectroscopy in peritumoral brain edema. *American Journal of Neuroradiology*. 2007; **28**: 1287–1291.

[44] Louis DN, Ohgaki H, Wiestler OD, Cavenee WK, *World Health Organization classification of tumours of the central nervous system*. IARC, Lyon. 2007.

[45] Barker II FG, Chang SM, Huhn SL, Davis RL, Gutin PH, McDermott MW, Wilson CB, Prados MD, Age and the risk of anaplasia in magnetic resonance-nonenhancing supratentorial cerebral tumors. *Cancer*. 2000; **80**: 936–941.

[46] McKnight TR, Lamborn KR, Love TD, Berger MS, Chang S, Dillon WP, Bollen A, Nelson SJ, Correlation of magnetic resonance spectroscopic and growth characteristics within grades II and III gliomas. *Journal of Neurosurgery*. 2007; **106**: 660–666.

[47] Stadlbauer A, Gruber S, Nimsky C, Fahlbusch R, Hammen T, Buslei R, Tomandl B, Moser E, Ganslandt O, Preoperative grading of gliomas by using metabolite quantification with high-spatial-resolution proton MR spectroscopic imaging. *Radiology*. 2006; **238**: 958–969.

[48] Jackson RJ, Fuller GN, Abi-Said D, Lang FF, Gokaslan ZL, Shi WM, Wildrick DM, Sawaya R, Limitations of stereotactic biopsy in the initial management of gliomas. *Neuro-Oncology*. 2001; **3**: 193–200.

[49] Law M, Yang S, Wang H, Babb JS, Johnson G, Cha S, Knopp EA, Zagzag D, Glioma grading: Sensitivity, specificity, and predictive values of perfusion MR imaging and proton MR spectroscopic imaging compared with conventional MR imaging. *American Journal of Neuroradiology*. 2003; **24**: 1989–1998.

[50] Di Costanzo A, Scarabino T, Trojsi F, Giannatempo GM, Popolizio T, Catapano D, Bonavita S, Maggialetti N, Tosetti M, Salvolini U, d'Angelo VA, Tedeschi G, Multiparametric 3T MR approach to the assessment of cerebral gliomas: tumor extent and malignancy. *Neuroradiology*. 2006; **48**: 622–631.

[51] Van Driessen K, Rousseeuw PJ, A fast algorithm for the minimum covariance determinant estimator. *Technometrics*. 1999; **41**: 212–223.

[52] Van Leemput K, Maes F, Vandermeulen D, Suetens P, Automated model-based bias field correction of MR images of the brain. *IEEE Transactions on Medical Imaging*. 1999; **18**: 885–896.

[53] Zha H, *The singular value decomposition theory, algorithms and applications*. Ph.D. thesis, Pennsylvania State University. 1993.

[54] Golub GH, Van Loan CF, *Matrix computations*. The Johns Hopkins University Press, Baltimore. 1996.

Appendix

Tumour segmentation based on outlier detection following (27)

The input for the algorithm, proposed in (27) by Prastawa *et al.*, is a probabilistic brain atlas and various MR images, although the T2-weighted MRI is the only required one. The method consists of three stages:

- *Detection of abnormality:*
  This stage aims to detect regions that deviate from normal, healthy brain. This involves finding the intensity parameters for the healthy tissue classes (i.e. white matter, gray matter and CSF) and the abnormal tissue. For this purpose a digital brain atlas is used. Specifically, the detection of abnormality is an iterative procedure that consists of the following steps:

(1) The posterior probabilities are thresholded in order to sample from high confidence regions. In the first iteration the atlas probabilities are used instead of the posterior probabilities.

(2) Since the samples for the healthy tissue classes contain unwanted samples from abnormal tissue classes, an outlier detection is performed based on the MCD method (51).

(3) For all tissue classes the probability density functions are estimated based on a non-parametric model using kernel expansions:

$$p(I(x)|y_j) = \frac{1}{N}\sum_{i=1}^{N} K_\lambda(I(x) - T_i), \tag{1}$$

with $I(x)$ the vector of MR intensities at location x, y_j the class label, K_λ the multivariate Gaussian kernel with standard deviation λ and T_i a tissue class training sample. Remark that the initial density for the abnormal tissue class is set to be uniform.

(4) Following Bayes rule the posterior probabilities are calculated:

$$p(y_j|I(x)) = \frac{p(I(x)|y_j)p(y_j)}{p(I(x))}, \tag{2}$$

while the priors, $p(y_j)$, for all classes are obtained from the corresponding atlas probabilities. The prior probabilities for abnormal tissue are set to a fraction of the sum of the probabilities for gray and white matter.

(5) The bias field is estimated from the probabilities of the gray and white matter classes (52). A correction is applied based on the estimated bias field.

- *Detection of edema:*
  It is assumed that the detected abnormal region mainly consists of tumour,

and possibly edema. First, the abnormal tissue is sampled based on the obtained posterior probabilities. The detection of edema stage assumes that edema appears brighter than tumour on the T2-weighted image. Therefore, a k-means clustering of these samples is performed and based on the Davies-Bouldin index, an overlap measure,

$$\frac{1}{2}\left(\frac{\frac{1}{m}\sum_{i=1}^{m}\|\tau_i-\mu_{tumour}\|+\frac{1}{n}\sum_{i=1}^{n}\|\epsilon_i-\mu_{edema}\|}{\|\mu_{tumour}-\mu_{edema}\|}\right), \tag{3}$$

it is determined whether there are separate clusters for tumour and edema. The mean value for the m candidate tumour samples τ_i is denoted by μ_{tumour} and the mean value for the n candidate edema samples ϵ_i is denoted by μ_{edema}. Next, the probability density functions for tumour and edema (if present) are estimated based on a non-parametric model using kernel expansions as explained before.

- *Reclassification with spatial and geometric constraints:*
  At this point, geometric and spatial constraints are included since the previous two steps generally result in a number of false positives. More specifically, this involves the pruning of samples before estimating the densities. The full iterative procedure during the third stage (of which part is similar to the first stage) consists of the following steps:

(1) The posterior probabilities are thresholded in order to sample from high confidence regions.
(2) The tumour samples are pruned using region competition snakes. The tumour posterior probabilities are used as input for the snake, which is represented by a zero level set. The snake expands when the boundary is inside the tumour and shrinks when the boundary encloses part of the regions not part of the tumour. For details about the implementation, the interested reader is referred to (30), explaining details about level set evolution with region competition.
(3) The edema samples are pruned with a neighbourhood test since it is assumed that the edema region is connected to a nearby tumour region. Edema samples can be located further away from the tumour, however, these samples have to be connected to a tumour region spatially.
(4) Similarly as before, the probability density functions are estimated based on a non-parametric model using kernel expansions.
(5) The posterior probabilities are calculated using Bayes rule.
(6) The bias field correction is applied.

Bayesian LS-SVM and pairwise coupling

The standard LS-SVM classifier has been introduced in (34):

$$\min_{w,b,e} \mathcal{J} = \mu \frac{1}{2} w^T w + \zeta \frac{1}{2} \sum_{i=1}^{N} {e_i}^2 \tag{4}$$
$$\text{subject to} \quad y_i(w^T \varphi(x_i) + b) = 1 - e_i, \quad i = 1, ..., N,$$

with training data $\{(x_i, y_i)\}, i = 1, ..., N$, where $x_i \in \mathbb{R}^d$ are the input data and $y_i \in \{-1, +1\}$ the matching class labels. In the primal space the unknown model is characterized by w, the bias term b and the error variable e_i. In the dual space the LS-SVM classifier is constructed by $y(x) = \text{sign}\left(\sum_{i=1}^{N} \alpha_i y_i K(x, x_i) + b\right)$, with x the case to be classified, α_i the Lagrange multipliers and $K(\cdot,\cdot)$ a positive definite kernel, i.e. the RBF kernel in this study.

In addition, a Bayesian evidence framework for LS-SVM classifiers has been established in (33). In general, this evidence framework makes use of three levels of inferences:

- first level

$$p(w, b|D, \log\mu, \log\zeta, H_\sigma) = \frac{p(D|w, b, \log\mu, \log\zeta, H_\sigma)}{p(D|\log\mu, \log\zeta, H_\sigma)} p(w, b|\log\mu, \log\zeta, H_\sigma) \tag{5}$$

- second level

$$p(\log\mu, \log\zeta|D, H_\sigma) = \frac{p(D|\log\mu, \log\zeta, H_\sigma)}{p(D|H_\sigma)} p(\log\mu, \log\zeta|H_\sigma) \tag{6}$$

- third level

$$p(H_\sigma|D) = \frac{p(D|H_\sigma)}{p(D)} p(H_\sigma) \tag{7}$$

with D being the data and H_σ the model depending on the RBF kernel parameter σ. At each level the Bayes rule is applied and the posterior is maximized.

The first level of inference determines the bias b and w of the LS-SVM model. On the second level the hyperparameters for regularisation (i.e. μ, ζ) are defined. The third level performs model comparison to infer the kernel parameters (i.e. σ).

The standard Bayesian LS-SVM method is a binary classifier that is able to calculate class probabilities. The study in (29) proposes to extend this binary Bayesian LS-SVM classifier to a multiclass Bayesian LS-SVM classifier using pairwise coupling of class probabilities. With this approach, the multiclass problem is divided into a number of binary problems following the one-versus-one approach. In order to retrieve multiclass class probabilities, the pairwise

probabilities of all binary classifiers are combined into multiclass class probabilities following the approach of Wu *et al.* (36). For this purpose, Wu *et al.* propose to solve the equations

$$\pi_i = \sum_{j:j\neq i} \left(\frac{\pi_i + \pi_j}{K-1} \right) \hat{\pi}_{ij}, \quad \forall i, \quad \sum_{i=1}^{K} \pi_i = 1, \quad \pi_i \geq 0, \tag{8}$$

using a linear system, with K the number of classes, π_i the probability that a case belongs to class i and π_{ij} (estimated by $\hat{\pi}_{ij}$) the probability that a case belongs to class i, conditional on the membership of class i or j.

Canonical correlation analysis

CCA represents the multivariate variant of ordinary correlation analysis, which quantifies the relationship between two random variables x and y by means of the so-called correlation coefficient ρ:

$$\rho = \frac{Cov[x,y]}{\sqrt{Var[x]Var[y]}}, \tag{9}$$

where $Cov[\cdot\,,\cdot\,]$ and $Var[\cdot\,]$ stand for covariance and variance, respectively. The correlation coefficient ρ is a scalar with value between -1 and 1 that measures the degree of linear dependence between x and y. For zero-mean variables equation (9) is replaced by:

$$\rho = \frac{E[xy]}{\sqrt{E[x^2]E[y^2]}}, \tag{10}$$

where $E[\cdot\,]$ stands for expected value. Canonical correlation analysis can be applied to multichannel signal processing as follows: consider two zero-mean multivariate random vectors $x = [x_1(t)...x_m(t)]^T$ and $y = [y_1(t)...y_n(t)]^T$, with $t = 1, ..., N$, where the superscript T denotes the transpose. The following linear combinations of the components in x and y are defined, which respectively represent two new scalar random variables Z_x and Z_y

$$\begin{aligned} Z_x &= \omega_{x_1} x_1 + ... + \omega_{x_m} x_m = \omega_x^T x, \\ Z_y &= \omega_{y_1} y_1 + ... + \omega_{y_n} y_n = \omega_y^T y. \end{aligned} \tag{11}$$

CCA computes the linear combination coefficients $\omega_x = [\omega_{x_1} \ ... \ \omega_{x_m}]^T$ and $\omega_y = [\omega_{y_1} \ ... \ \omega_{y_n}]^T$, called regression weights, so that the correlation between the new variables Z_x and Z_y is maximum. The solution $\omega_x = \omega_y = 0$ is not allowed and the new variables Z_x and Z_y are called canonical variates. Several implementations of CCA are available in the literature. However, as shown in (12), the most reliable and fastest implementation is based on the interpretation of CCA in terms of principal angles between linear subspaces (53, 54). For further details, the reader is referred to (12) and references therein.

Kernel logistic regression

In (32), it has been shown that multiclass KLR can be solved by using an iteratively re-weighted version of LS-SVMs. Suppose the data set consists of N samples with an input vector $x_i \in \mathbb{R}^d$, $i = 1, ..., N$, where the first element of x_i is 1 and an outcome y_i indicates to which of the K outcome classes the sample belongs. The common method to infer the model parameters, $\beta_b, b = 1, ..., K-1$, for the multiclass logistic regression model is using a penalized negative log-likelihood (NLL):

$$\text{NLL} + \frac{\gamma}{2} \sum_{b=1}^{K-1} (\beta_b)^T \beta_b, \tag{12}$$

with the Kth class the reference class. Assuming that $B = [\beta_1^T \ ... \ \beta_{K-1}^T]^T \in \mathbb{R}^{(K-1)d}$, a vector with all model parameters, the Newton-based optimization strategy is used:

$$B^{(k)} = B^{(k-1)} + s^{(k)}. \tag{13}$$

The vector $B^{(k)}$ contains the parameter estimates at iteration k and the step, $s^{(k)}$, is $-[H^{(k)}]^{-1} g^{(k)}$ where the gradient and Hessian of the penalized NLL are respectively defined as g and H. To express multiclass KLR in terms of iteratively re-weighted LS-SVMs, define $\phi^T \in \mathbb{R}^{(K-1)q \times (K-1)N}$ as

$$\phi^T = \left[\begin{array}{ccc|ccc|c|ccc} \varphi(x_1) & 0 & 0 & \varphi(x_2) & 0 & 0 & & \varphi(x_N) & 0 & 0 \\ 0 & \ddots & 0 & 0 & \ddots & 0 & \cdots & 0 & \ddots & 0 \\ 0 & 0 & \varphi(x_1) & 0 & 0 & \varphi(x_2) & & 0 & 0 & \varphi(x_N) \end{array}\right],$$

where $\varphi : \mathbb{R}^d \to \mathbb{R}^q$ is a mapping from the input space to the feature space, induced by a positive definite kernel. Next define $r_n = [I_{(y_i=1)} \ ... \ I_{(y_i=K-1)}]^T$,

$R = [r_1^T \ ... \ r_N^T]^T$, $P^{(k)} = [p_{1,1}^{(k)} \ ... \ p_{K-1,1}^{(k)} \ ... \ p_{1,N}^{(k)} \ ... \ p_{K-1,N}^{(k)}]^T \in \mathbb{R}^{(K-1)N}$ and the ith block ($\in \mathbb{R}^{(K-1)\times(K-1)}$) of the blockdiagonal weight matrix $W^{(k)} = \text{blockdiag}(W_1^{(k)} \ ... \ W_N^{(k)})$ as

$$W_i^{(k)} = \begin{bmatrix} t_i^{1,1} & t_i^{1,2} & \cdots & t_i^{1,K-1} \\ t_i^{2,1} & t_i^{2,2} & & t_i^{2,K-1} \\ \vdots & & \ddots & \\ t_i^{K-1,1} & t_i^{K-1,2} & & t_i^{K-1,K-1} \end{bmatrix},$$

with

$$t_i^{a,b} = \begin{cases} p_{a,i}^{(k)}(1 - p_{a,i}^{(k)}), & \text{if } a = b \\ -p_{a,i}^{(k)} p_{b,i}^{(k)}, & \text{if } a \neq b \end{cases}$$

Next, within the context of LS-SVMs the following primal problem is minimized

$$\begin{aligned} \min_{s^{(k)}, e^{(k)}} \ & \frac{1}{2}(e^{(k)})^T W^{(k)} e^{(k)} + \frac{\gamma}{2}(s^{(k)} + B^{(k-1)})^T (s^{(k)} + B^{(k-1)}) \\ & \text{subject to } (W^{(k)})^{-1}(R - P^{(k)}) = \phi s^{(k)} + e^{(k)}, \end{aligned} \tag{14}$$

where e^k is an error variable at iteration k. In the dual space the solution for the problem in equation (14) can be obtained by solving a linear system. The class probability of a new case x^* for class a, following the multiclass KLR model, can be obtained by

$$\frac{\exp\left[(\beta_a)^T \varphi(x^*)\right]}{\sum_{b=1}^{K} \exp\left[(\beta_b)^T \varphi(x^*)\right]}, \tag{15}$$

where $(\beta_a)^T \varphi(x^*) = \frac{1}{\gamma} \sum_{i=1, i\in\mathcal{D}_a}^{N} \alpha_{i,a} K(x_i, x^*)$, with $\mathcal{D}_a$ the training data belonging to class a, $\alpha_{i,a}$ the support value for the prediction of class a for case i and $K(x_i, x^*) = \varphi(x_i)^T \varphi(x^*)$ a positive definite kernel function (i.e. RBF kernel).

Table 1
Pathology, tumour grade, age and sex for 11 subjects.

Case	Pathology	Grade	Age	Sex
1	diffuse astrocytoma	II	57	male
2	diffuse astrocytoma	II	58	female
3	diffuse astrocytoma	II	39	male
4	oligoastrocytoma	II	42	male
5	oligodendroglioma	II	48	female
6	oligodendroglioma	II/III	41	female
7	oligodendroglioma	III	30	female
8	glioblastoma	IV	53	male
9	glioblastoma	IV	54	male
10	glioblastoma	IV	50	male
11	meningioma	I	45	female

Captions of figures

Figure 1: Mean water-normalized magnitude MR spectra for normal tissue, CSF, grade II gliomas, grade III gliomas, meningiomas and glioblastomas. The solid lines are the means, while the dotted lines are the means plus the standard deviations.

Figure 2: From left to right: the T2-weighted MRI for case 6, the ratio of choline over creatine and the probabilities generated by the LDA classifier for abnormal tissue. The lighter the map is, the higher the ratio or probabilities.

Figure 3: Case 9, glioblastoma. Top row: T1-weighted image, T2-weighted image, proton density-weighted image and gadolinium enhanced T1-weighted image. Bottom row: T2-weighted image, nosologic image, MR spectra located in the box shown in the T2-weighted image on the left. Light blue reflects white matter, dark blue gray matter, green csf, yellow grade II glioma, orange grade III glioma, dark red glioblastoma and purple meningioma.

Figure 4: Top row: case 8, glioblastoma. T2-weighted image and nosologic image. Bottom row: case 10, glioblastoma. T2-weighted image and nosologic image. The hematoma for case 10 is identified by an arrow.

Figure 5: Case 4, grade II glioma. Top row: T1-weighted image, T2-weighted image, proton density-weighted image and gadolinium enhanced T1-weighted image. Bottom row: T2-weighted image, nosologic image, MR spectra located in the box shown in the T2-weighted image on the left. The arrows identify the enhanced area.

Figure 6: Case 6, grade II/III glioma. Top row: T1-weighted image, T2-weighted image, proton density-weighted image and gadolinium enhanced T1-weighted image. Bottom row: T2-weighted image, nosologic image, MR spectra located in the box shown in the T2-weighted image on the left. The arrow identifies the enhanced area.

Figure 7: Case 7, grade III glioma. Left: T2-weighted MR image, right: nosologic image.

Figure 8: Case 3, grade II glioma. Top row: T1-weighted image, T2-weighted image, proton density-weighted image and gadolinium enhanced T1-weighted image. Bottom row: T2-weighted image, nosologic image, MR spectra located in the box shown in the T2-weighted image on the left.

Figure 9: Top row: case 2, grade II glioma. Proton density-weighted image and nosologic image. Bottom row: case 11, meningioma. T1-weighted image and nosologic image.

Figure 10: Case 5, grade II glioma. From left to right: T2-weighted MR image, nosologic image obtained by KLR, nosologic image obtained by thresholding the KLR output. The pixels with probabilities higher than 60 % are kept, while the remaining ones are left black.

Figure 11: Top row: case 6, grade III glioma. Probability map and contour plot. Grade III glioma probabilities are higher at the frontal part of the abnormal tissue region with the enhancement after gadolinium and smaller at the occipital part of the tumour. Bottom row: case 7, grade III glioma. Map of correlation coefficients obtained with CCA and contour plot. The correlation coefficients are higher in the center and at the medial part of the tumour.

Figure 12: Samples picked for the normal tissue classes (i.e. gray matter, white matter and CSF) using the digital brain atlas during the detection of abnormality step. The T2-weighted MR images for cases 1, 4, 5 and 6, from top to bottom, are depicted on the left. The images in the middle depict the samples that are chosen based on the original segmentation algorithm described in (27). The images on the right show the sampling result by including a subject-specific abnormal tissue prior, causing less sample contamination.

Figure 13: The effect of using a subject-specific abnormal tissue prior based on MRSI for case 4. The results on the left are generated without an abnormal tissue prior in contrast to the results on the right. The top row shows the prior probabilities from the atlas, the bottom row the final segmentation result. The abnormal tissue is only correctly recognized by the segmentation algorithm that includes the extra abnormal tissue prior from MRSI.

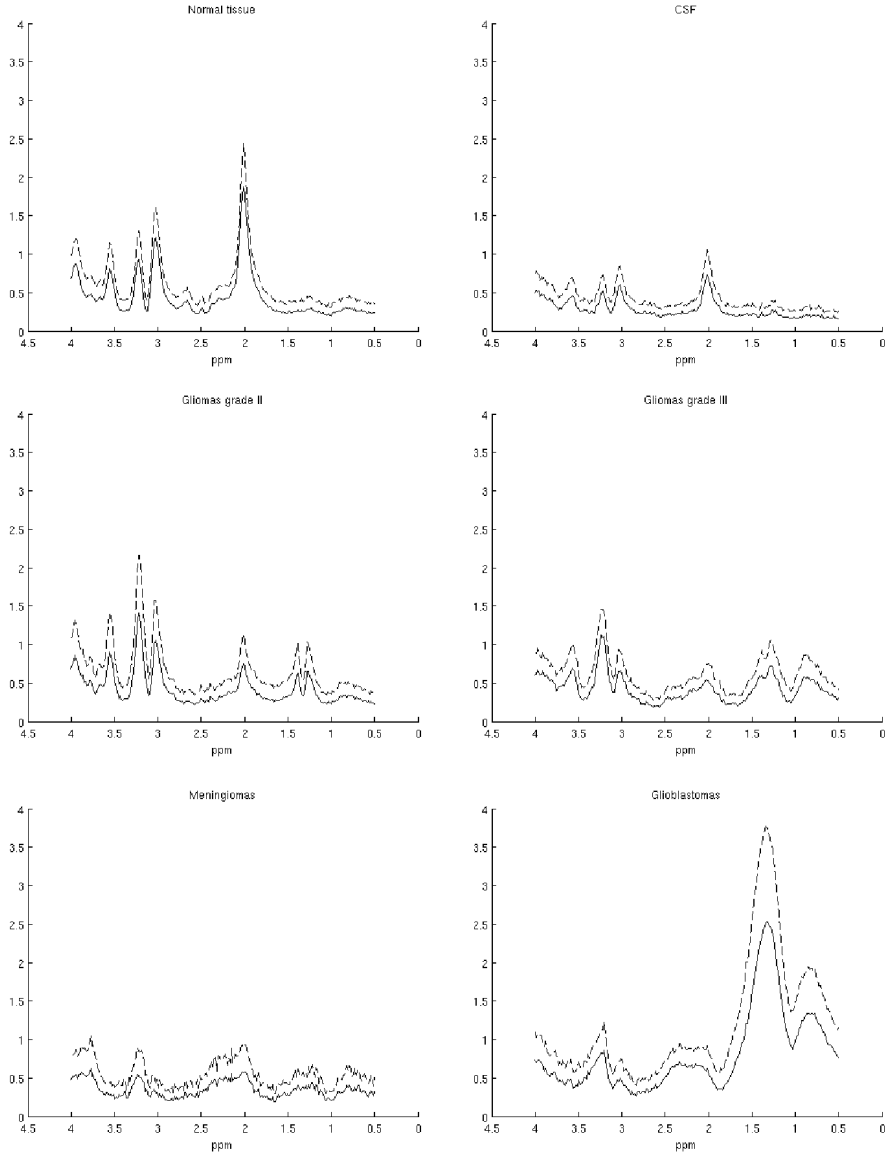

Fig. 1. Luts *et al.*

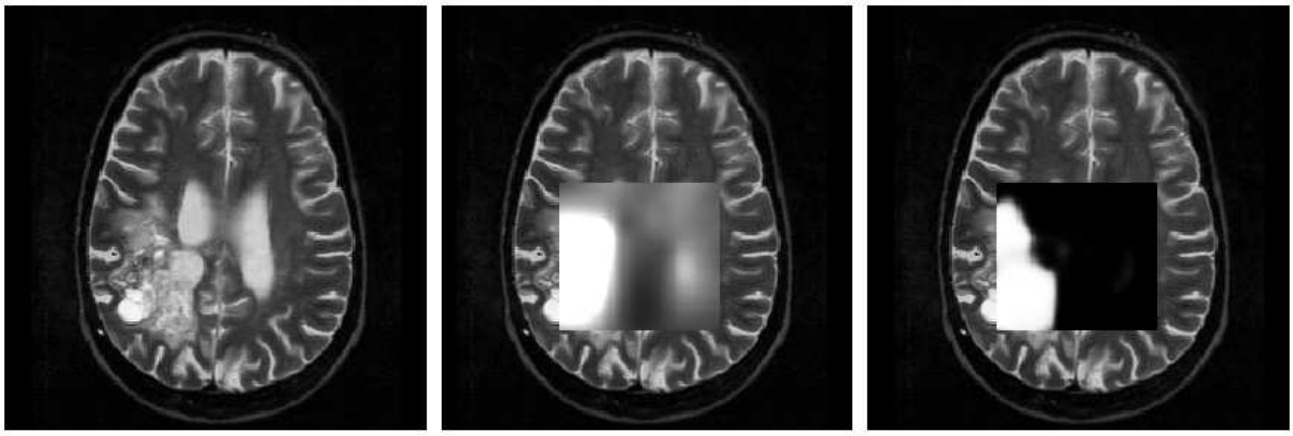

Fig. 2. Luts *et al.*

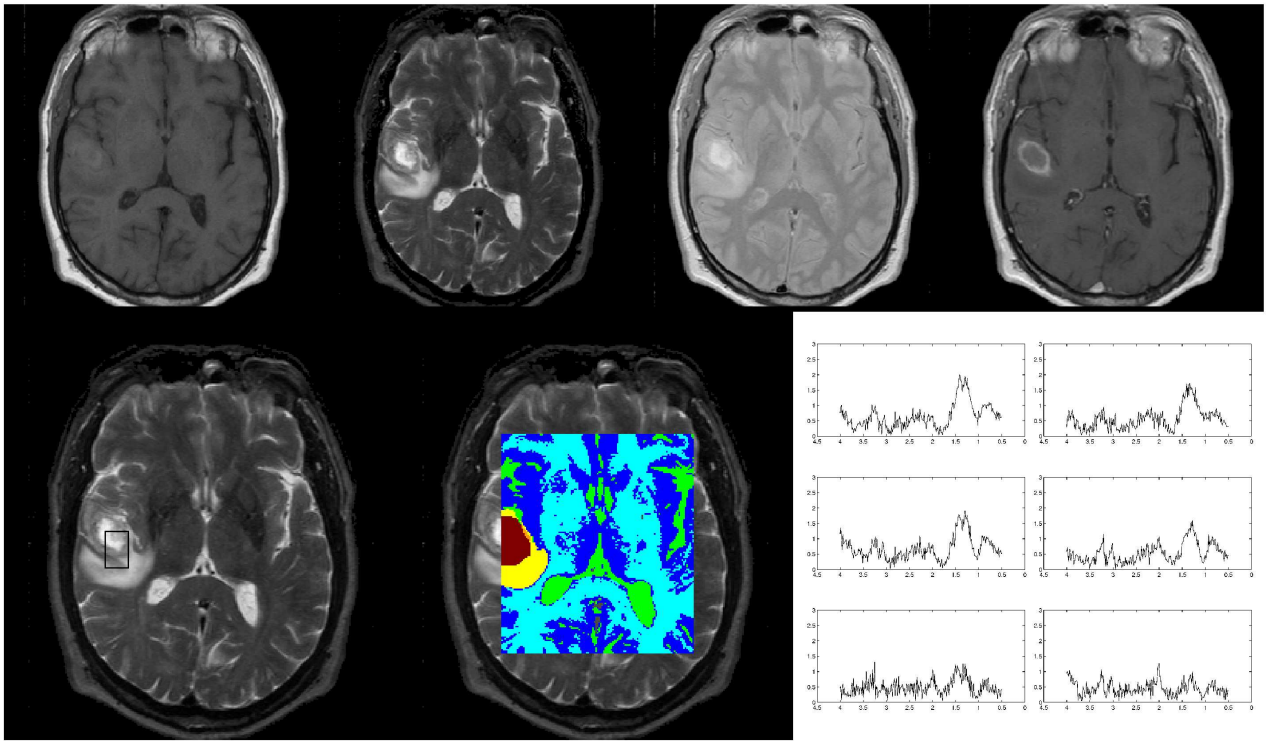

(a) *case 9*

Fig. 3. Luts *et al.*

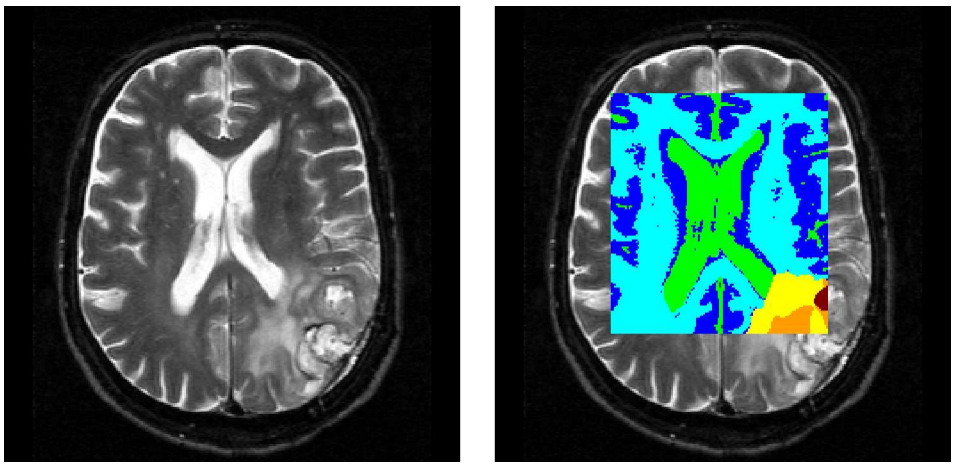

(a) *case 8*

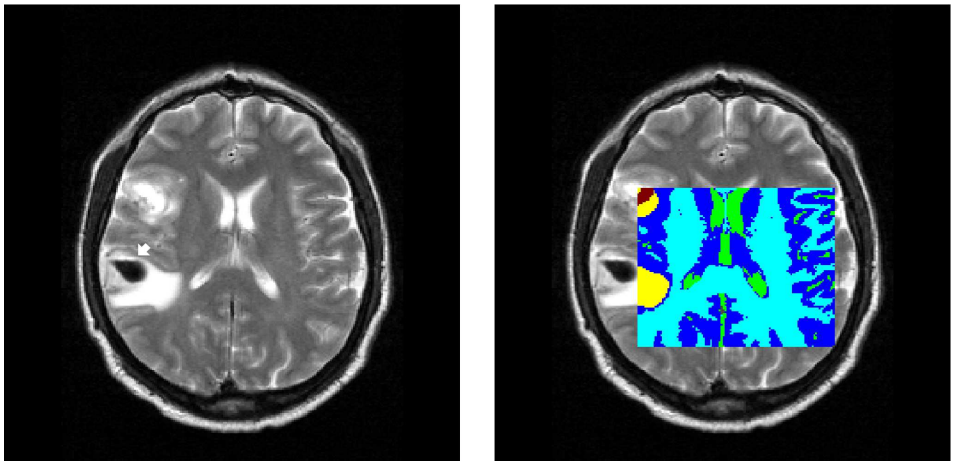

(b) *case 10*

Fig. 4. Luts *et al.*

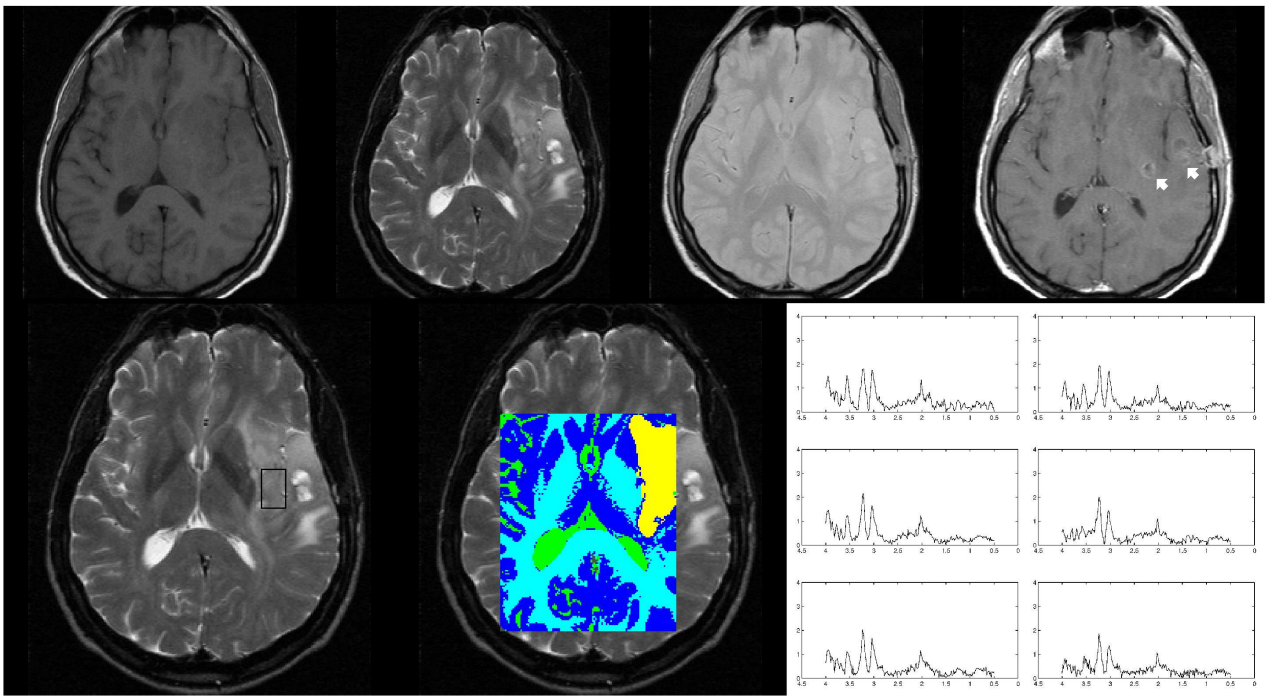

(a) *case 4*

Fig. 5. Luts *et al.*

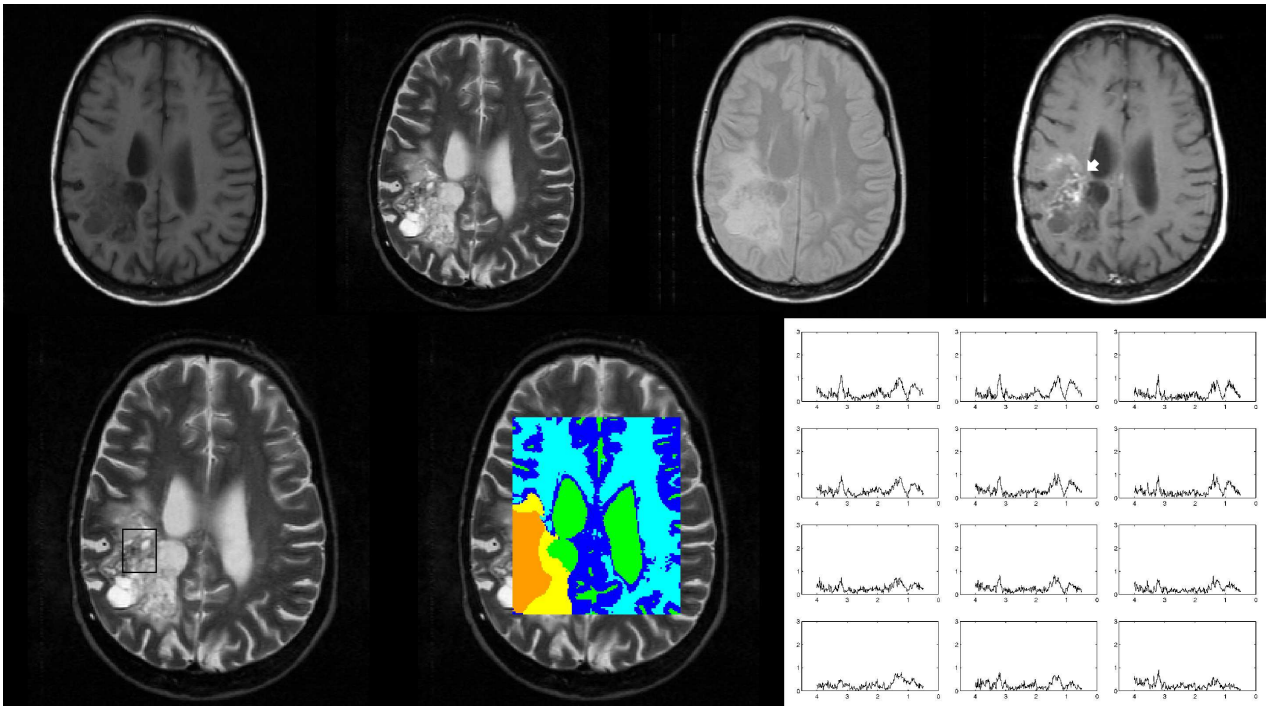

(a) *case 6*

Fig. 6. Luts *et al.*

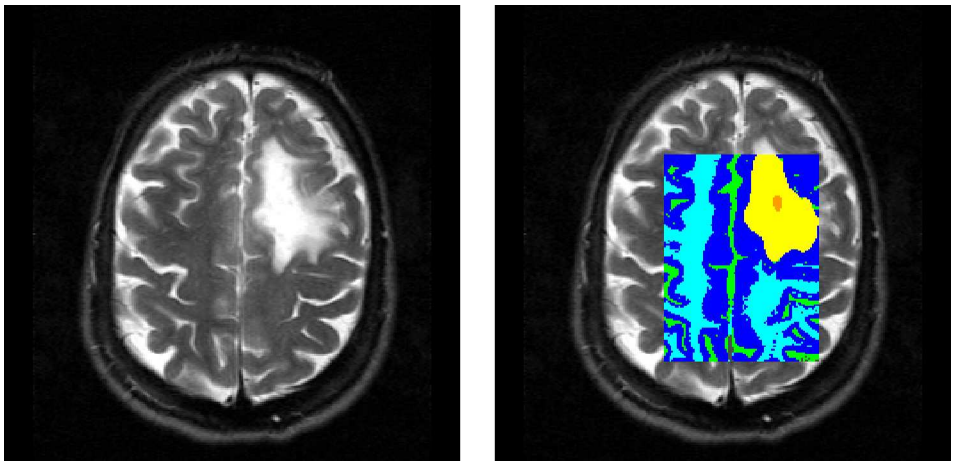

(a) *case 7*

Fig. 7. Luts *et al.*

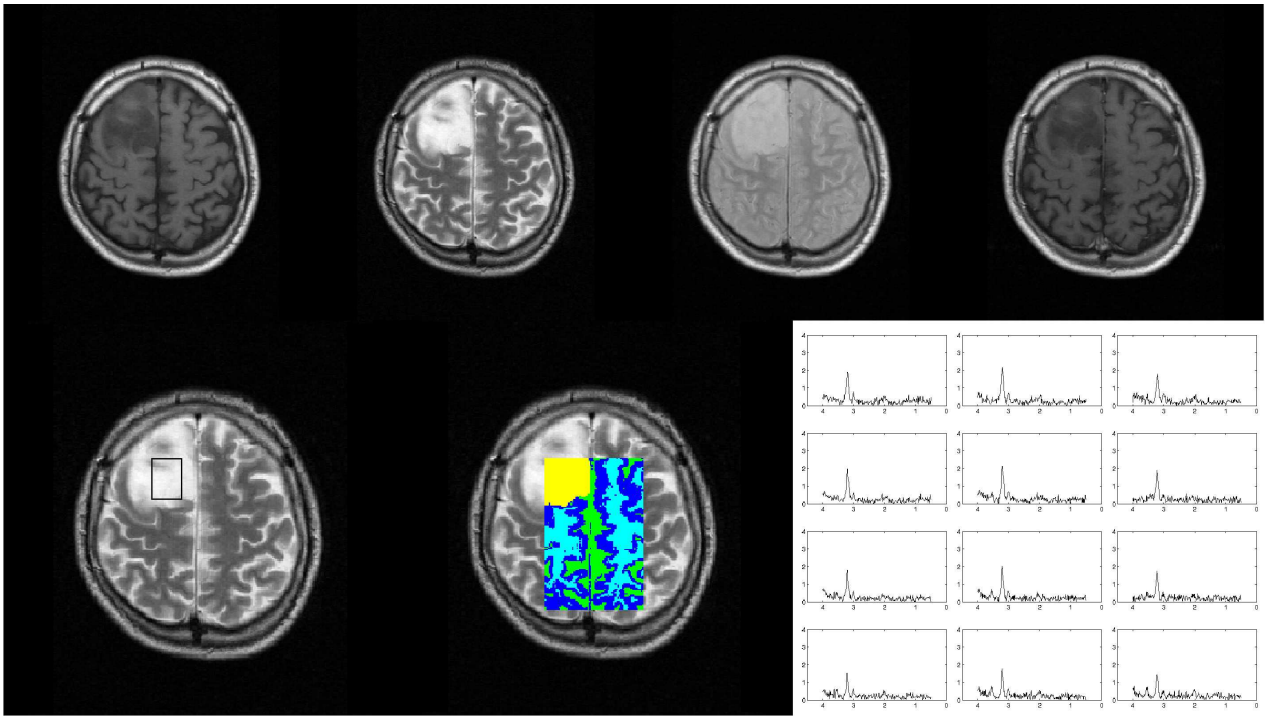

(a) *case 3*

Fig. 8. Luts *et al.*

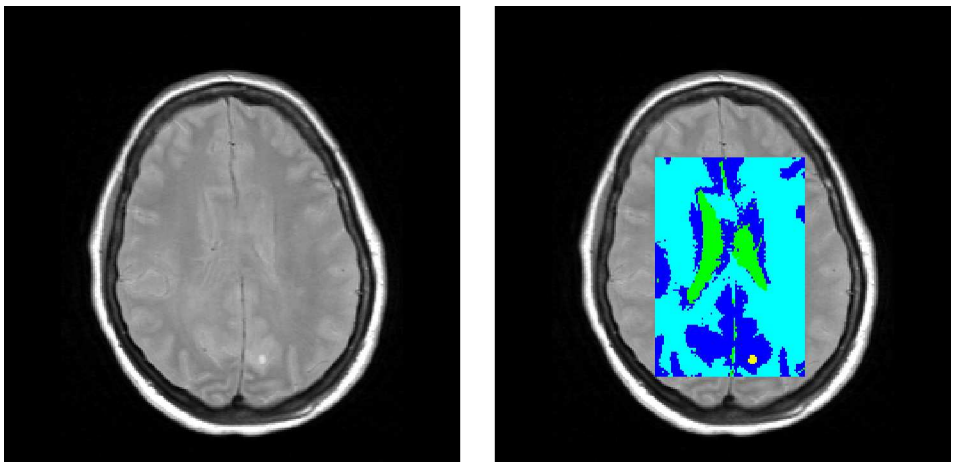

(a) *case 2*

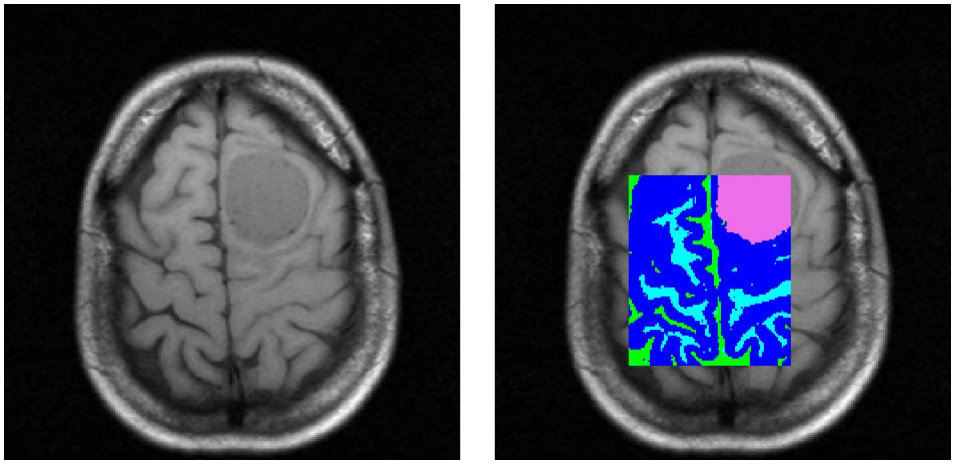

(b) *case 11*

Fig. 9. Luts *et al.*

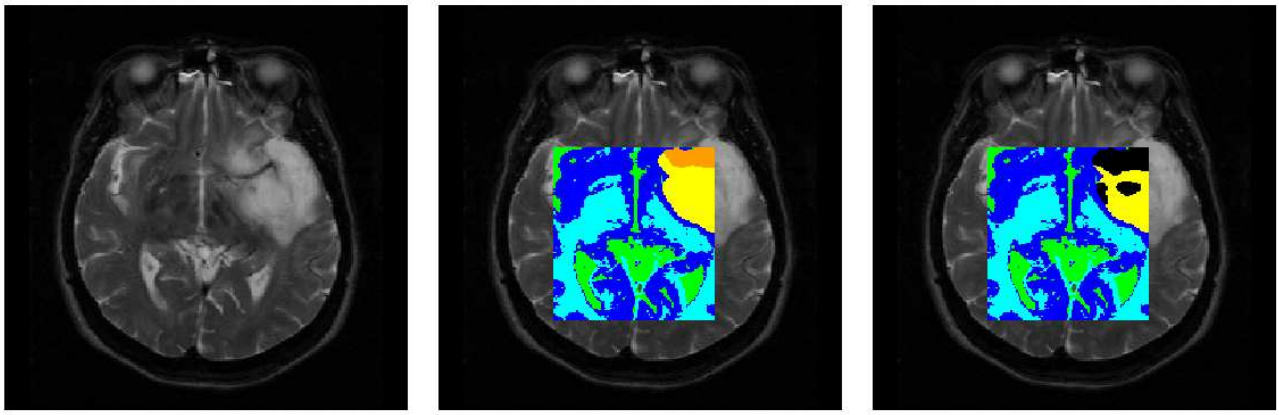

(a) *case 5*

Fig. 10. Luts *et al.*

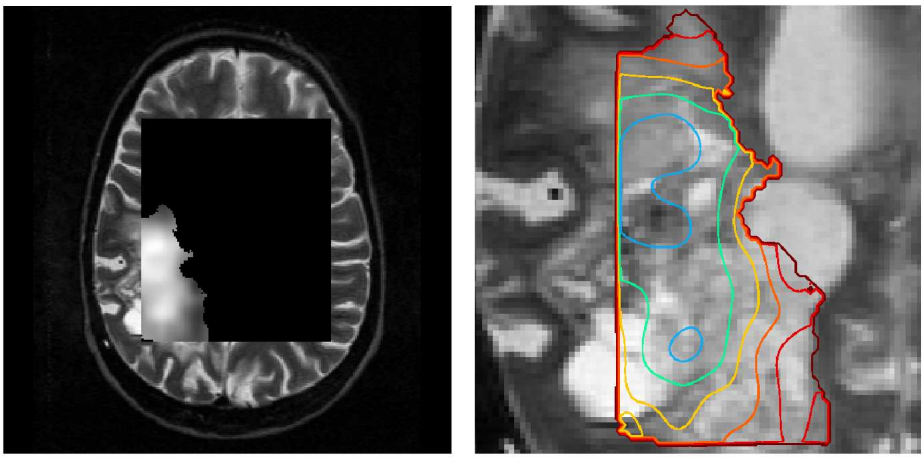

(a) *case 6*

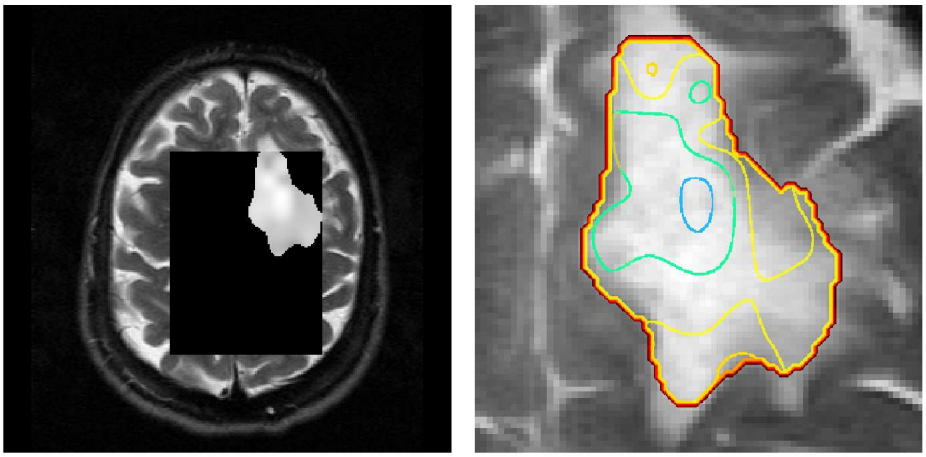

(b) *case 7*

Fig. 11. Luts *et al.*

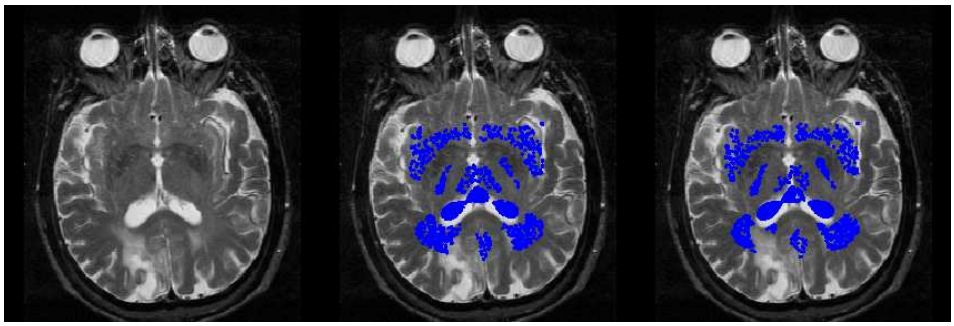

(a) *case 1*

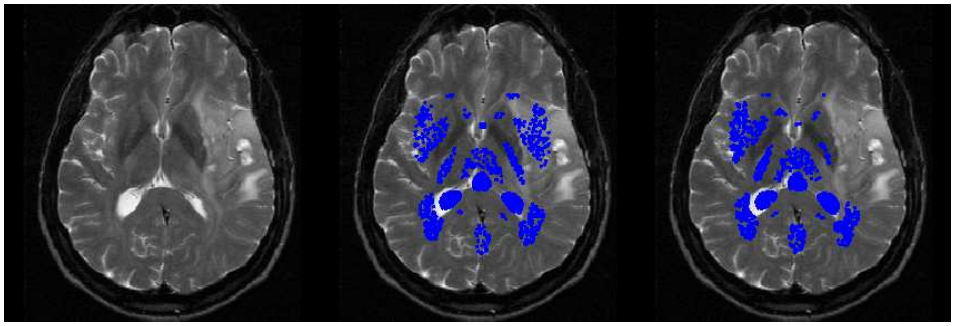

(b) *case 4*

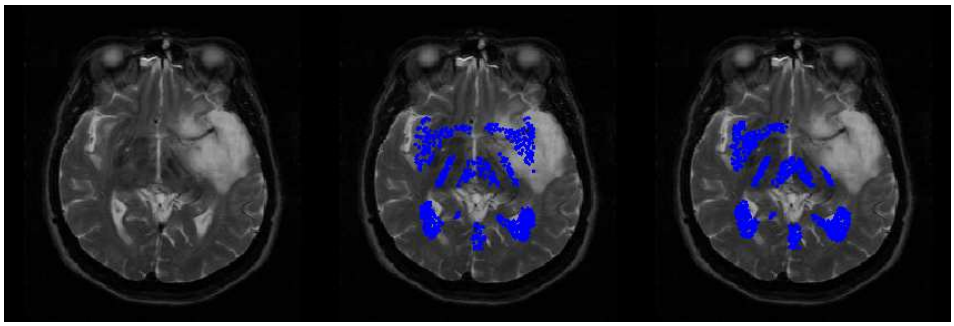

(c) *case 5*

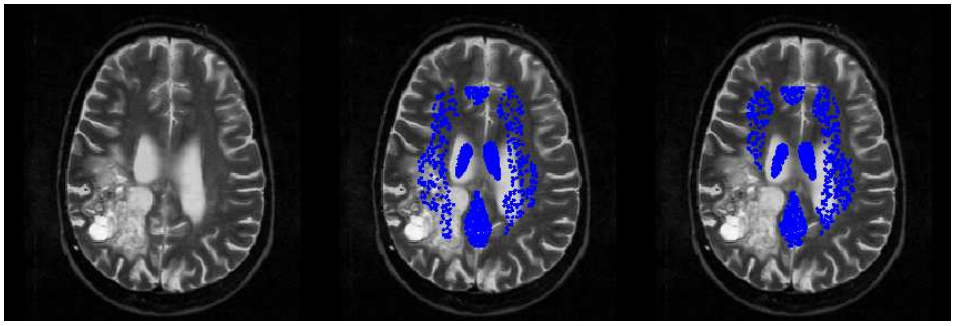

(d) *case 6*

Fig. 12. Luts *et al.*

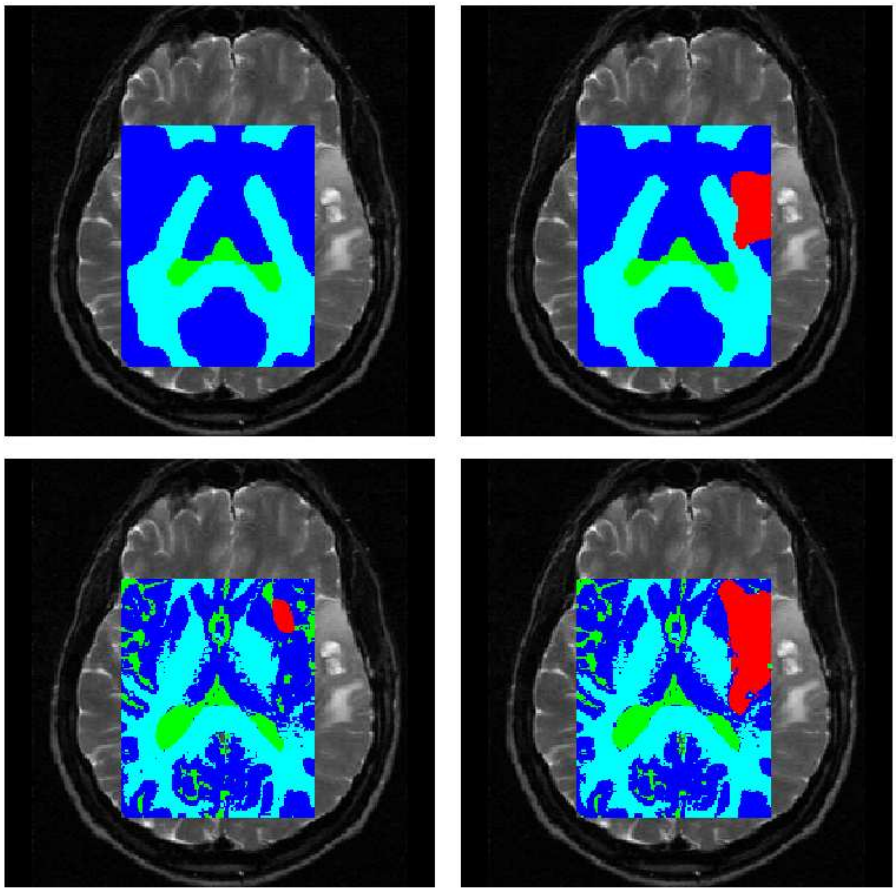

(a) *case 4*

Fig. 13. Luts *et al.*